CIRP Annals - Manufacturing Technology 74 (2025) 309–313

Contents lists available at ScienceDirect

CIRP Annals - Manufacturing Technology

journal homepage: https://www.editorialmanager.com/CIRP/default.aspx

Laser powder bed fusion process parameters for the fabrication of unsupported overhang structures of metamaterial lattices

Wessel W. Wits (2)[a,b,*], Camill de Vos[a], Maria Montero-Sistiaga[a], Marc de Smit[a]

[a] NLR – Royal Netherlands Aerospace Centre, Marknesse, The Netherlands
[b] Faculty of Electrical Engineering, Mathematics and Computer Science, University of Twente, Enschede, The Netherlands

ARTICLE INFO

Article history:
Available online 4 April 2025

Keywords:
Additive manufacturing (AM)
Powder bed fusion (PBF)
Metamaterials

ABSTRACT

Laser powder bed fusion of unsupported overhang structures, required for metamaterial lattices, are difficult to manufacture. In this study, process parameters are experimentally determined to successfully fabricate auxetic re-entrant metamaterial structures. Due to the support-less printing, higher linear energy densities compared to contour and hatch scanning are required to build continuously solidified overhang structures. Simulation results show that the melt pool width and in particular the length is enlarged, promoting loose powder attachment by denudation and balling. Auxetic re-entrant metamaterials are successfully fabricated. Impact tests show good mechanical performance and better energy absorption compared to previous studies.

1. Introduction

Metamaterials are artificial structural designs capable of achieving unprecedented properties not observed in naturally occurring materials. These extraordinary materials have complex, small repeating structures, i.e., unit cells, that can be designed to exhibit unique properties, such as a negative refractive index, perfect absorption, negative thermal conductivity or negative Poisson's ratio. The ability to create such materials has far-reaching implications for various fields including aerospace, defence, energy, biomedical, optics, and more [1,2].

The development of Additive Manufacturing (AM) technologies has revolutionised amongst others the field of metamaterials by enabling the efficient and economic production of complex geometries that were previously impossible to manufacture using traditional methods. AM offers unparalleled flexibility in geometry coverage from macro-scale to micro-scale, local tailorability and free-form capabilities [3,4]. The adoption of AM for metamaterials opens up new avenues for research and development [5,6]. By leveraging advantages of AM, complex structures with predefined optical, acoustic and mechanical properties can be designed and fabricated [7]. Mechanical metamaterials typically feature counterintuitive mechanical properties besides the constituent material arising from the architecture of the unit cell [8].

Recent studies have examined several AM-fabricated mechanical metamaterials. For high-energy absorption, a number of ideal structures have been identified [9,10]. For instance, stretch-dominated structures, such as the octet truss, have unique strength-to-weight characteristics exceptional for energy absorption purposes. For large deformability, an auxetic structure, such as the strut-based re-entrant lattice, features an advantageous negative Poisson's ratio; however, its unit cell is difficult to manufacture. Laser Powder Bed Fusion (LPBF) is notorious for its limitations in fabricating unsupported overhang structures [11], which are required to fabricate auxetic re-entrant structures, as shown in the right-hand side inset of Fig. 1.

To warrant LPBF processability, overhang structures are typically designed following a minimum (material-specific) inclination angle or otherwise they are given a support structure that needs to be remove afterwards. For metamaterials in which the unit cell is repeated numerous times, post-process removal of supports is not a feasible approach. To solve this, researchers have adapted the unit cell design to improve manufacturability; e.g., overhanging struts have been replaced by 45° inclined struts or support material has been included into the unit cell as a compromise [12,13]. Also, demanded metamaterial behaviour has been modelled in the *x-y* plane and then continuously fabricated as a thin-walled honeycomb structure in the *z*-direction, i.e. a 2D metamaterial [14]. Both approaches are suboptimal as most proposed metamaterial structures, e.g. to attain auxetic behaviour, require a lattice design that includes overhang structures.

LPBF processing maps, as generalised in Fig. 1, are generally used to identify suitable Regions of Interest (ROIs). The defect-free ROI is bound by regions prone to keyhole defects, balling and lack-of-fusion defects [15]. Furthermore, within the defect-free ROI, typical parameter sets are developed for subtle contour scanning and faster hatch scanning. In this study, we aim to find a parameter set that would allow for the unconstrained fabrication of overhanging struts within a lattice structure. Normally the melt pool of the laser scan track has to reach the underlying previously solidified material through the deposited powder bed layer to guarantee a good build. In doing so also a thermal path is created through which the melt pool can conduct its excess heat and rapidly solidify [16]. The goal is to find the ROI where the melt pool is solidified as a horizontal unsupported overhang structure spanning a relatively short distance between 4 and 8 mm, as is typically found in the unit cell design of metamaterial structures.

* Corresponding author.
E-mail address: w.w.wits@utwente.nl (W.W. Wits).

https://doi.org/10.1016/j.cirp.2025.03.003

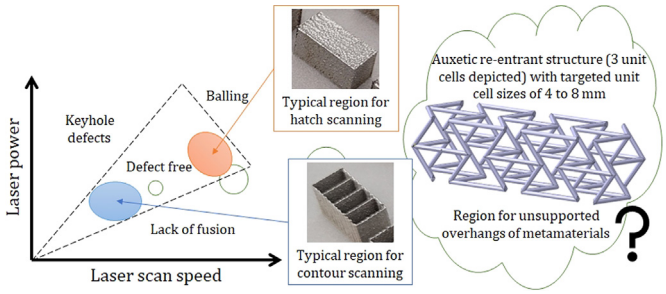

Fig. 1. Generalised laser power vs. scan speed LPBF processing map; insets highlight typical regions of interest based on supported builds, yet for unsupported overhangs, typical for metamaterials, this is unknown.

2. Modelling and experimental approach

To understand the solidification behaviour and dimensions of a single laser scan track based on selected LPBF process parameters, several mathematical models have been proposed in the literature. Typically, the size of the melt pool is computed and used as a starting point to predict scan track dimensions. For instance, Tang et al. [17] proposed a relatively simple equation based on the Rosenthal equation in which the melt pool geometry is computed based on the laser power and scan speed in combination with a number of material and powder bed parameters. Rubenchik et al. [18] proposed a refined model by including the Eagar-Tsai temperature fields model [19] and developed scaling laws to compute the melt pool geometry based on dimensionless numbers p and B. Letenneur et al. [20] validated a similar analytical model specifically for stainless steel 316 L, which is also the material of choice for this study. In their model, the laser beam energy is modelled on a semi-infinite solid representing the powder bed. The laser beam irradiating the powder bed is modelled as a Gaussian beam and is assumed to illuminate the surface of the powder bed for a time interval defined by the laser scan speed and the laser spot size. The temperature distribution within the powder bed caused by the laser energy can be modelled as [20]:

$$T(x,y,z) = T_0 + \frac{A_{PB}P}{\frac{1}{2}dk_{PB}\pi^{\frac{3}{2}}} \int_{-\infty}^{0} \frac{1}{1+\tau^2} e^{-\frac{\tau^2}{1+\tau^2}\left(\left(\xi-\frac{Pe}{2\tau^2}\right)^2+\eta^2\right)-\tau^2\zeta^2} d\tau \quad (1)$$

with: $\xi = 2\sqrt{2}\frac{x}{d}$, $\eta = 2\sqrt{2}\frac{y}{d}$, $\zeta = 2\sqrt{2}\frac{z}{d}$, $Pe = \frac{dv}{4\sqrt{2}\alpha_{PB}}$, $\tau = \frac{d}{4\sqrt{2\alpha_{PB}t}}$

Here, T_0 is the initial powder bed temperature controlled by the LPBF-preheating temperature, which was set to 150 °C for this study. A_{PB} is the material-specific absorptivity [-] of the laser energy by the powder bed. P and d are the laser power [W] and spot diameter [m], respectively. k_{PB} is the material-specific thermal conductivity [W/m·K] of the powder bed. (ξ, η, ζ) coordinates are normalised (x, y, z) Cartesian coordinates by the laser beam diameter. *Pé* is the Péclet number [-] relating advective to diffusive heat transfer within the powder bed. v is the travel speed of the melt pool [m/s], which is assumed equal to the scan speed of the laser beam along the x-axis. The time constant τ is normalised taking the laser spot size, the thermal diffusivity and the process time t [s] into account. Finally, α_{PB} is the thermal diffusivity [m^2/s] of the powder bed, which is defined as:

$$\alpha_{PB} = \frac{k_{PB}}{\rho_{PB}c_{p,PB}} \quad (2)$$

where, ρ_{PB} and $c_{p,PB}$ are the density [kg/m^3] and specific heat capacity [J/kg·K] of the powder bed, respectively.

The material properties of the powder bed are derived from SS316L bulk properties at the melting temperature of 1400 °C and by applying a scaling factor determined by the effective powder bed density, which is material and recoater specific. Table 1 lists the SS316L powder bed properties used for this study, derived by applying an experimentally determined scaling factor of 0.7. The laser absorptivity and laser spot diameter are modelled as 0.5 and 85·10^{-6} m, respectively.

Table 1
SS316L powder bed parameters for the melt pool prediction.

Parameter	Symbol	Value
Density	ρ_{PB}	5527 kg/m^3
Thermal conductivity	k_{PB}	23.2 W/m·K
Specific heat capacity	$c_{p,PB}$	512.2 J/kg·K

To compute the melt pool geometry, the computational domain is set to a size of 600 µm along the laser scan direction (x-axis), 300 µm across (y-axis) and 100 µm powder bed thickness (z-axis). Due to the Gaussian model, the temperature distribution is symmetrical along the scan direction. The origin of the coordinate system is aligned with the centre of the laser spot illuminating the top surface of the powder bed and the laser scan direction is in negative x direction. To distinguish the melt pool, the locally computed temperatures are maximised to the melting temperature of 1400 °C for SS316L [20]. For temperatures above this threshold value, the material is assumed to be in the molten state. Fig. 2 shows the computational domain and illustrates a typical melt pool geometry from which the melt pool width and depth, as well as the tail length, can be determined. The laser spot is illustrated in yellow. In this exemplary case, the simulated melt pool is 128 µm (2 × 64 µm) wide, 54 µm deep and 190 µm long.

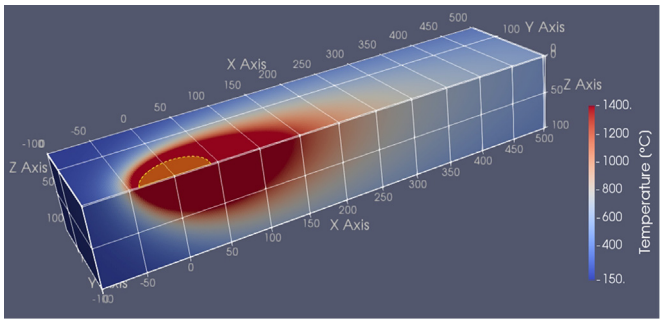

Fig. 2. Computational domain [µm] to simulate the melt pool geometry dark red indicates material (SS316L) in the molten state (i.e. the melt pool) and the yellow dashed line indicates the laser spot.

Goal of the experimental campaign is to determine optimal process parameters for the fabrication of horizontally overhanging struts without any supporting structure. For this, a novel approach has been devised in which overhangs are laser scanned between two pillars of 4x Ø0.5 mm, as illustrated in Fig. 3(a); thus, mimicking the horizontal struts of an auxetic re-entrant lattice. The laser system is programmed such that each overhang is scanned in one continuous motion from one pillar to the other. In this way, one continuous melt track is created rather than e.g. two tracks that meet somewhere in between. The overhang is constructed by laser scanning five single scan tracks on top of each other with a recoating step in between similar to regular LPBF fabrication. Before each recoating step, the build platform is lowered 50 µm. The power and scan speed are systematically varied from 110 to 290 W, and 370 to 970 mm/s, respectively, as indicated in the process window of Fig. 3(b). Next, the distance between the two pillars is increased from 4 to 8 mm in steps of 1 mm. In this way, 500 combinations are tested in total.

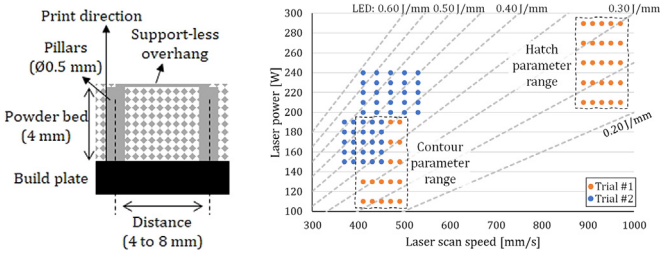

a) experimental approach b) design of experiments

Fig. 3. LPBF fabrication of overhangs without support structure.

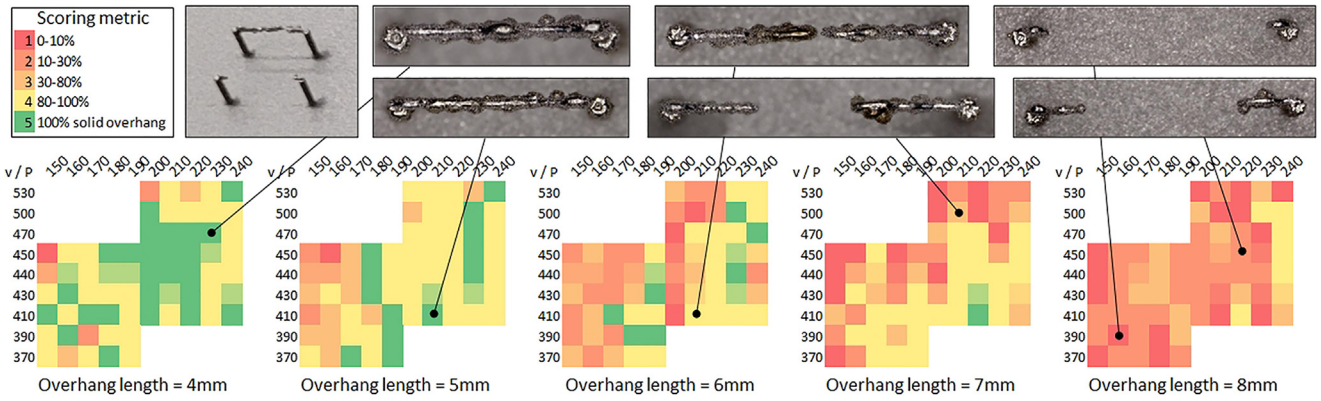

Fig. 4. Result of fabricating horizontal overhang structures without supports; inserts are exemplary images to understand the scoring metric.

The experiment was conducted in two steps. First, the experimental design focused around the previously determined optimal working points for contour scanning and hatch scanning indicated by the orange points in Fig. 3(b). Second, the focus area shifted to higher Linear Energy Densities (LEDs), defined as the ratio of laser power to scan speed, at relatively low scan speeds, as indicated by the blue points in Fig. 3(b). The experimental trials were conducted on an SLM Solution 280HL machine using stainless steel 316 L as powder feedstock material. Optical analysis was conducted using a Keyence VHX-1000 digital light microscope. The quality of each overhang structure was evaluated by visual inspection. A score of 1 (hardly any structure visible at all) up to 5 (continuously solidified overhang) was applied. The scoring metric including exemplary images are shown in the top of Fig. 4. The size (i.e. the width) of the fabricated overhang structures was determined from a top-view observation.

3. Simulation and experimental results

To validate the numerical model, first the width of thin wall structures is predicted and compared to an earlier test campaign that focused on finding optimal contour scanning parameters by stacking single scan tracks on top of each other (see bottom centre inset of Fig. 1). The width of the thin walls was determined by optical cross-sectional analysis. The measured widths are depicted as black dots in Fig. 5. The vertical spread is caused by the tested range of laser power-scan speed combinations, as well as process variation (i.e. noise). The blue area represents the simulation results in which the vertical spread is also caused by the simulated combinations of laser power and scan speed. The figure illustrates that the model using the material parameters of Table 1 is well capable of predicting the width of single scan tracks. Fig. 5 also shows the simulation results for the higher LEDs matching the process window of Trial #2. As expected, continuously wider structures are predicted for a higher energy input.

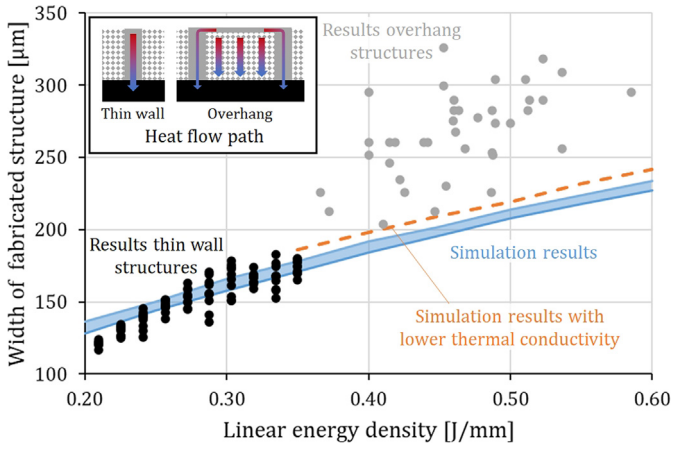

Fig. 5. Measured (dots) and simulated (blue area) width of thin wall (black) and horizontal overhang (grey) structures; inset illustrates the difference in heat flow path for thin wall and overhang structures.

Trial #1 resulted in the fabrication of few successful overhang structures. Some successful overhangs were found in the top left-hand side of the contour parameter range (see Fig. 3). Hence, in Trial #2 the focus was expanded in this direction with higher LEDs. The results of the Trial #2 are illustrated in Fig. 4. As can be expected, best results are found for the shortest overhang distance of 4 mm. For each increment in overhang length, the number of completely solidified overhangs is lower. For an overhang distance of 8 mm, none of the laser power-scan speed combinations led to the formation of a completely solidified overhang. In total Trial #2 produced 39 successful overhang structures out of 250 tested combinations. Although it is expected that below 4 mm even more successful overhangs can be fabricated, for such short lengths the unit cell will collide internally and not render auxetic behaviour.

The measured width of each successfully consolidated overhang structure is depicted in Fig. 5 by the grey dots. Most successful overhangs are fabricated with a LED between 0.40–0.55 J/mm; higher than conventionally applied values for contour or hatch scanning of SS316L. Most successful overhangs (10 out of 39) were fabricated with a scan speed of 410 mm/s. Similar to the model prediction, the experimental results display a befitting trend that higher LEDs lead to wider overhang structures. The model however underpredicts the width by about 70 µm on average.

One explanation discussed earlier is the fact that consolidating on powder, compared to solid structures, causes poor thermal conduction downwards to the base plate. Although the applied scaling factor corrects for powder bed material properties, the effect of a thick poorly conducting powder bed is not well taken into account. In fact, the effective thermal conductivity of a powder bed may be 1,000x lower compared to bulk material [21]. Hereto, the thermal conductivity, k_{PB}, and hence the thermal diffusivity, α_{PB}, according to Eq. (2), are adjusted. Assuming the conductivity is correct for supported structures, as is the case for the afore-examined thin wall structures, a geometry-based parallel thermal resistance network can be constructed to model heat transfer through both the powder bed and the two 4x Ø0.5 mm pillars towards the base plate (see Fig. 5 inset). Following the approach of Lee et al. [21], the effective conductivity of a SS316L powder bed was measured to be 0.32 W/m·K. By implementing this value in a thermal resistance network model, for the shortest overhang structure of 4 mm an equivalent thermal conductivity of 4.90 W/m·K can be computed, almost 5x lower than the value of Table 1. The effect of applying a lower thermal conductivity on the melt pool width is indicated by the orange dashed line in Fig. 5. Results show that indeed the melt pool width is enlarged; however, altogether the melt pool width remains underpredicted.

The fabricated overhang structures exhibit a large number of unfused powder particles attached to the overhang, which can also be seen from the insets of Fig. 4. Due to the fact that fabrication is done directly on the powder bed without solid supports, heat dissipation towards the build plate is hampered. This results in relatively high melt pool temperatures, which is known to induce a lateral gas flow towards the melt pool [22]. This gas flow may entrain powder particles drawing them into the melt pool, associated to the denudation process. Next to the high number of unfused particles, the denudation effect also explains the relatively high width of the overhang

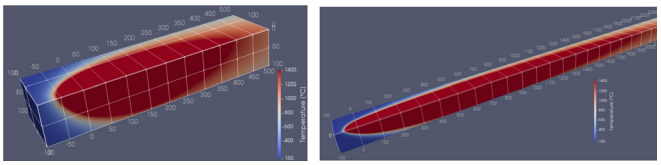

a) Regular thermal conductivity, k_{PB}, of 23.2 W/m·K b) Overhang-adjusted thermal conductivity, k_{PB}, of 4.90 W/m·K

Fig. 6. Simulation results of the melt pool geometry [µm] at a scan speed of 450 mm/s and a LED of 0.45 J/mm.

structures, approximately 3x the laser spot diameter, as powder is cleared around the scan track and brought into the melt pool. The overhang structures also exhibit the effect of balling, which is known to occur when fabricating without solid support, due to overheating of the melt pool [23]. Melt pool hot spots drive Marangoni flow thereby inducing circulatory motion in the melt pool. An elongated melt pool, as is the case for low thermal dissipation, may also lead to balling due to Plateau-Rayleigh type instabilities [24].

To understand the model underpredictions, Fig. 6 compares the melt pool geometry for the regular and overhang-adjusted thermal conductivity. Both the scan speed and LED are selected mid-way the tested range at 450 mm/s and 0.45 J/mm, respectively. For the overhang-adjusted case, the computational domain had to be enlarged along the scan direction to determine the melt pool dimensions. For the regular value, see Fig. 6(a), the melt pool width is 200 µm (2 × 100 µm), while in the overhang-adjusted case of Fig. 6(b) the melt pool is wider: 210 µm. The increase in width of about 10 µm is constant for all LEDs, as can also be seen in Fig. 5. However, Fig. 6(b) also shows that, due to the poor thermal contact through the powder bed, the melt pool is profoundly extended along the scan direction. The simulated length of the regular melt pool is 444 µm, while for the overhang-adjusted melt pool the length is 4x longer (1885 µm). The reason why mainly the length is affected is because of the adapted time constant τ in Eq. (1) impacting the temperatures in the scan direction. As mentioned, elongated melt pools are prone to balling.

The simulation results indicate that the predicted maximum melt pool width is mainly restricted by the laser spot diameter. Even at low conductivity and the highest LED, the melt pool width does not grow beyond 242 µm. Instead, the excessive energy causes the melt pool to be markedly elongated. Without thresholding at the melting temperature, the simulated temperatures are also much higher for the lower thermal conductivity case. As the theoretical model is conduction based, the simulation results fall outside the validated range and are not accurate enough to predict the melt pool geometry even with an adjusted thermal conductivity value. As also demonstrated by Bayat et al., neglecting the fluid flow leads to unrealistically large melt pools [25]. Hence, in order to correctly simulate the fabricated overhang structures, the model should be extended to include fluid dynamics, and convective and radiative heat transfer contributions, due to the high melt pool temperatures, alongside temperature-dependent material properties. Also, the afore-discussed denudation effect drawing in more powder particles should be incorporated.

4. Metamaterial fabrication

Based on the results of Fig. 4, a maximum unit cell size of 6 mm is selected for the fabrication of an auxetic re-entrant metamaterial in which support-less horizontal overhangs are present. By overlaying the results for the 4, 5 and 6 mm overhang lengths, six parameter sets give best results. The parameter set of 410 mm/s scan speed and 170 W laser power is selected, as the corresponding LED of 0.41 J/mm is closest to the contour scanning parameter set. This is a good compromise between the horizontal overhangs and inclined struts that are both present in the auxetic re-entrant lattice. Also, the total energy input will be relatively low avoiding excessive balling and denudation.

Fig. 7 depicts a top view of the fabricated overhang structures for the 4 mm and 6 mm lengths, as well as a photograph of the fabricated metamaterial lattice. A section of the auxetic re-entrant metamaterial was impact tested using a drop-weight tester. The dynamic stress-strain behaviour of the metamaterial showed progressive resistance as can be

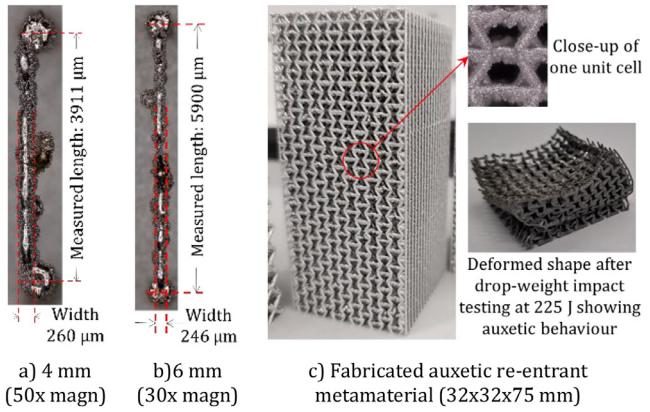

a) 4 mm (50x magn) b)6 mm (30x magn) c) Fabricated auxetic re-entrant metamaterial (32x32x75 mm)

Fig. 7. Overhang structures and corresponding metamaterial build fabricated using 410 mm/s laser scan speed and 170 W laser power.

expected from an auxetic material. Moreover, the experimentally determined specific energy absorption between 8.0–10.3 kJ/kg for SS316L is higher than other reported sources [9–10]. In a separate study, quasi-static compression testing was performed, in which auxetic behaviour was observed as well. Near-instant collapses of a complete layer did not occur. Hence, although some balling and loose powder attachment are present in the overhang structures, the solidified truss structures are capable of transferring the required loads to enable the structure to successfully act as an auxetic metamaterial.

5. Conclusions

LPBF process parameters have been determined for the fabrication of unsupported overhanging struts required for auxetic re-entrant metamaterials. Following a novel experimental design, single overhang structures were systematically fabricated, and the resulting quality and size were measured. For SS316L best results are obtained with a higher LED compared to conventional process parameters. Complete metamaterial structures were additively fabricated and impact tested to determine the energy absorption behaviour. Both successful load transfer through the metamaterial structure as well as auxetic material behaviour were observed.

In future work, other scan strategies for support-less printing; e.g., variable laser process parameters, laser defocusing, zig-zagging rather than straight line scanning, etc., are to be explored. These strategies may suppress the effect of balling and result in longer continuously solidified, yet unsupported overhangs.

Declaration of competing interest

The authors declare that they have no known competing financial interests or personal relationships that could have appeared to influence the work reported in this paper.

CRediT authorship contribution statement

Wessel W. Wits: Writing – original draft, Visualization, Validation, Software, Methodology, Investigation, Formal analysis, Data curation, Conceptualization. **Camill de Vos:** Writing – review & editing, Resources, Project administration, Funding acquisition. **Maria Montero-Sistiaga:** Writing – review & editing, Methodology, Conceptualization. **Marc de Smit:** Writing – review & editing, Methodology, Funding acquisition, Conceptualization.

Acknowledgements

The authors acknowledge the support of the European Union's Horizon Europe Research and Innovation Programme under grant agreement No 101046835 for the in-depth thermal analysis of powder and powder bed properties for, amongst others, LPBF processes.

References

[1] Kadic M, Milton GW, Van Hecke M, Wegener M (2019) 3D metamaterials. *Nature Review Physics* 1(3):198–210.
[2] Holliman JE, Schaef HT, McGrail BP, Miller QRS (2022) Review of foundational concepts and emerging directions in metamaterial research: design, phenomena, and applications. *Material Advances* 3(23):8390–8406.
[3] Thompson MK, et al. (2016) Design for Additive manufacturing: trends, opportunities, considerations, and constraints. *CIRP Annals* 65(2):737–760.
[4] Bourell D, et al. (2017) Materials for additive manufacturing. *CIRP Annals* 66 (2):659–681.
[5] Wegener K, et al. (2023) Biologicalisation in manufacturing – Current state and future trends. *CIRP Annals* 72(2):781–807.
[6] Askari M, et al. (2020) Additive manufacturing of metamaterials: a review. *Additive Manufacturing* 36:101562.
[7] Fan J, et al. (2021) A review of additive manufacturing of metamaterials and developing trends. *Materials Today* 50:303–328.
[8] Wu X, Su Y, Shi J (2019) Perspective of additive manufacturing for metamaterials development. *Smart Materials and Structures* 28(9):093001.
[9] Li Y, Jiang D, Zhao R, Wang X, Wang L, Zhang L-C (2024) High mechanical performance of lattice structures fabricated by additive manufacturing. *Metals (Basel)* 14(10).
[10] Zhang P, Yu P, Zhang R, Chen X, Tan H (2023) Grid octet truss lattice materials for energy absorption. *International Journal of Mechanical Sciences* 259:108616.
[11] Zwier MP, Wits WW (2016) Design for additive manufacturing: automated build orientation selection and optimization. *Procedia CIRP* 55:128–133.
[12] Xiong J, Gu D, Chen H, Dai D, Shi Q (2017) Structural optimization of re-entrant negative Poisson's ratio structure fabricated by selective laser melting. *Material and Design* 120:307–316.
[13] Li S, Hassanin H, Attallah MM, Adkins NJE, Essa K (2016) The development of TiNi-based negative Poisson's ratio structure using selective laser melting. *Acta Materilia* 105:75–83.
[14] Stanczak M, Fras T, Blanc L, Pawlowski P, Rusinek A (2021) Numerical and experimental study on mechanical behaviour of the AlSi10Mg aluminium structures manufactured additively and subjected to a blast wave. *EPJ Web of Conferences* 250:02017.
[15] Agrawal AK, Rankouhi B, Thoma DJ (2022) Predictive process mapping for laser powder bed fusion: a review of existing analytical solutions. *Current Opinion in Solid State and Materials Science* 26(6):101024.
[16] Wits WW, Bruins R, Terpstra L, Huls RA, Geijselaers HJM (2016) Single scan vector prediction in selective laser melting. *Additive Manufacturing* 9:1–6.
[17] Tang M, Pistorius PC, Beuth JL (2017) Prediction of lack-of-fusion porosity for powder bed fusion. *Additive Manufacturing* 14:39–48.
[18] Rubenchik AM, King WE, Wu SS (2018) Scaling laws for the additive manufacturing. *Journal of Materials Processing Technology* 257:234–243.
[19] Eagar TW, Tsai NS (1983) Temperature fields produced by traveling distributed heat sources. *Welding Journal* 62(12):346–355.
[20] Letenneur M, Kreitcberg A, Brailovski V (2019) Optimization of laser powder bed fusion processing using a combination of melt pool modeling and design of experiment approaches: density control. *Journal of Manufacturing and Materials Processing* 3(1). Art. no. 1.
[21] Lee H, Koutsioukis A, Jafari D, Geurts BJ, Wits WW (2024) Measurement of effective thermal conductivity of composite powders of 2D materials and metals for additive manufacturing. *Journal of Physics: Conference Series* 2766(1):012186.
[22] Matthews MJ, Guss G, Khairallah SA, Rubenchik AM, Depond PJ, King WE (2016) Denudation of metal powder layers in laser powder bed fusion processes. *Acta Materilia* 114:33–42.
[23] Lindström V, Lupo G, Yang J, Turlo V, Leinenbach C (2023) A simple scaling model for balling defect formation during laser powder bed fusion. *Additive Manufacturing* 63:103431.
[24] Zöller C, Adams NA, Adami S (2023) Numerical investigation of balling defects in laser-based powder bed fusion of metals with Inconel 718. *Additive Manufacturing* 73:103658.
[25] Bayat M, Mohanty S, Hattel JH (2019) A systematic investigation of the effects of process parameters on heat and fluid flow and metallurgical conditions during laser-based powder bed fusion of Ti6Al4V alloy. *International Journal of Heat and Mass Transfer* 139:213–230.